GRADUATE SCHOOL

3D Printing and Mechanical Performance of Silicone Elastomers

A THESIS
SUBMITTED TO THE FACULTY OF THE GRADUATE SCHOOL
OF THE UNIVERSITY OF MINNESOTA

by

Noah James Holzman

IN PARTIAL FULFILLMENT OF THE REQUIREMENTS
FOR THE DEGREE OF
MASTER OF SCIENCE

Advisor: Lorraine Francis

October 2019

Acknowledgements

Thanks to my friends and family for the love and support during my undergraduate and graduate career. Thanks to the CEMS community, which has been wonderful in supporting my academic, personal and professional development. Thanks to my advisor, Lorraine Francis, for her unwavering support and patience during my journey in graduate school.

Abstract

3D printing of soft, elastomeric materials has potential to increase the accessibility while decreasing the cost of customizable soft robotics and biomedical devices. In this work, the steps to building a 3D printer capable of printing with an extrudable liquid are described. A moisture-cure room temperature vulcanizing (RTV) silicone elastomer was 3D printed. The relative density of printed specimens was determined as a function of infill density specified in the software and the relationship was found to be non-linear and dependent on the sample geometry. Printed test specimens with a range of infill densities and several infill geometries were characterized under uniaxial tension and compression. In tension, the stress-strain behavior is non-linear over the entire curve. Ultimate tensile strength was relatively unaffected by infill density over a range of relative densities from 0.35 to 1.0, while extension at break decreased with increasing infill density. The apparent Young's modulus was determined in the small-strain limit and is tunable from 310-1150 kPa by adjusting the infill density. Tensile strength of fully-dense printed samples (1150±30 kPa) is comparable to that of the bulk cast samples (1150±40 kPa), indicating good performance of the printing process and few defects. In compression, three different infill patterns and a range of infill patterns were tested. The specimens exhibit stress-strain behavior typical of foams—a linear elastic region with a modulus dependent on infill density, followed by a buckling plateau region and densification at high strains. Negative stiffness due to snap-through buckling was observed in some cases. Results for both tension and compression tests show the tunability of mechanical response achievable through changing the software infill density.

Table of Contents

List of Figures

List of Tables

1. Introduction to 3D Printing

3D printing (3DP) is a category of additive manufacturing (AM)[1]. 3DP offers geometric complexity and customizability that is not available in other fabrication techniques. Parts with hollow interiors, undercuts and internal channels are not possible or very difficult to achieve with injection molding, pressing or casting. This complexity comes at no added cost; multi-piece molds are not required to make complex shapes. 3D printing is now a widely implemented method of manufacturing, particularly for prototyping and limited run parts. 3D printing is now a multibillion dollar market[2].

Thermoplastics for 3DP are already highly developed and 3D printers are available at both consumer and commercial levels. Although typically associated with hard thermoplastics, interest in incorporating other materials into 3DP to utilize their functional properties is increasing. Silicone elastomers are not a readily available feedstock for 3D printers. Currently, there are few commercial options available for silicones and the material selection is limited to a few traditional ceramics such as clay and porcelain. This works aims to further develop silicone elastomers for the 3D printing process, forward the understanding of how machine and feedstock parameters affect print quality, then applying this fundamental knowledge to explore the range of mechanical properties that can be achieved by 3D printing elastomers.

The term "3D printing" incorporates multiple different additive manufacturing techniques. The most common are fused deposition modelling (FDM), stereolithography and material jetting. However, all of them have the common fundamental inputs that directly relate to the quality of the final part; the material, the machine and the computer control system.

The technique used in this work was first known as "robocasting" and was developed in the early 1990's at Sandia National Lab as a method to print ceramic slurries or pastes[3]. In robocasting, a syringe pump is attached to a three-axis motion stage. The syringe, filled with a highly-loaded ceramic slurry, is pressured (mechanically in the original embodiment) and the slurry is forced out through a nozzle to deposit material in a controlled fashion in the XY plane. After completion of a single XY layer, the Z-axis is moved up to deposit the next layer. The process is repeated until the part is fully build up.

Despite having the major advantage of robocasting to use virtually any material, it took over 10 years before the method gained traction with other materials. The robocasting technique largely failed efforts at commercialization for unknown reasons. In the early 2010's, researchers began to experiment with the development of metallic colloidal "inks" for electronic applications and hydrogel-based inks for biological applications. Robocasting then became more commonly known as "direct-ink write" or DIW printing but has been given other names as well[4]. Here, the term "liquid deposition modelling" or LDM will be used.

At this point, 3D printing was becoming a household name, partly due to the expiration of original patents, the commoditization of components used in 3D printers and efforts by open-source and nonprofit groups (such as the RepRap project[5]) to build free software for printers.

The lack of standardization among 3D printer manufacturers and standards organizations is a significant problem still faced by the otherwise promising methods. For example, commercial machines often use custom firmware or proprietary slicers for their machines. This makes it difficult to compare the effectiveness across machines since a researcher would need a large amount of capital to purchase or use each machine.

Standards organizations (e.g. ASTM or ISO) have also trailed on developing ways to assess 3D printed parts. This makes it difficult to compare 3D printed parts to bulk material properties as there are no specific guidelines on how parts should be fabricated with 3D printing.

The two problems are approached by using off-the-shelf parts to construct an inexpensive liquid deposition printer and open-source software that is readily available online. This combination significantly lowers the cost to entry, increasing the accessibility and providing a powerful platform to those interested in liquid deposition modelling. To aide in standardization, all machine parameters, schematics and details such as the pressure-time response of the system that have been omitted from previous reports are included and described in detail. Methods to create reliable and repeatable results for mechanical testing are also described.

In this thesis, a liquid extrusion 3D printing apparatus is described and used to create novel silicone materials. Silicone-based polymers are of particular interest due the their high flexibility, biocompatibility, hydrophobicity as well as chemical and thermal resistance[6]. Therefore, the potential for applications in regenerative medicine [7], soft robotics [8] and human-electronic interface devices [9,10] warrant study of the process fundamentals and means of tailoring the mechanical properties. Chapter 2 introduces the liquid extrusion 3D printing process and provides background concerning the mechanical properties of 3D printed silicones. Chapter 3 provides the experimental methods for specimen preparation and chapter 4 gives the methods of mechanical characterization and results. Finally, conclusions are provided in chapter 5.

2. Liquid Extrusion 3D Printing

Liquid extrusion printers are often custom built due to the limited availability of commercial solutions and the expense of those on the market. Here, a first principles approach is taken to modify a normal 3D printer frame and gantry with open-source electronic and pneumatic system. The approach described herein is germane to any 3D printing frame regardless of the kinematic system (i.e. the gantry system, whether that is a classic cartesian style printer, “delta” (Stinson platform), polar or CoreXY operated platform, it is a matter of coordinate conversion to the relevant kinematic setup. The basic variables of the system and geometry are shown in Figure 2.1 below.

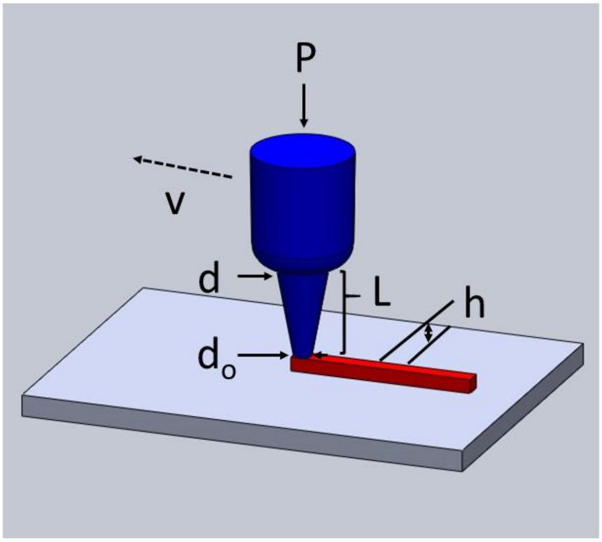

P = applied pressure
v = toolhead velocity
d = diameter of die entry
d_o= diameter of die exit
L = length of die
h = height of slice

Figure 2.1: Schematic of printer and relevant variables.

3D printing toolpath generation software (referred to as a slicer due to the layer-by-layer build process) allows a user to define many parameters. The number of shells or perimeters controls how many extrusions make up the outer walls of a part, which determines the wall thickness. Infill dictates how internal sections of the part are printed and affects the properties of the part, print time and material usage. The infill density can be varied from 0 percent (hollow) to 100 percent (fully dense), effectively controlling the porosity. The infill pattern affects how the space is filled; three patterns used in this study are shown in Figure 2.2. These complex internal patterns are not easily fabricated with traditional manufacturing processes such as injection molding

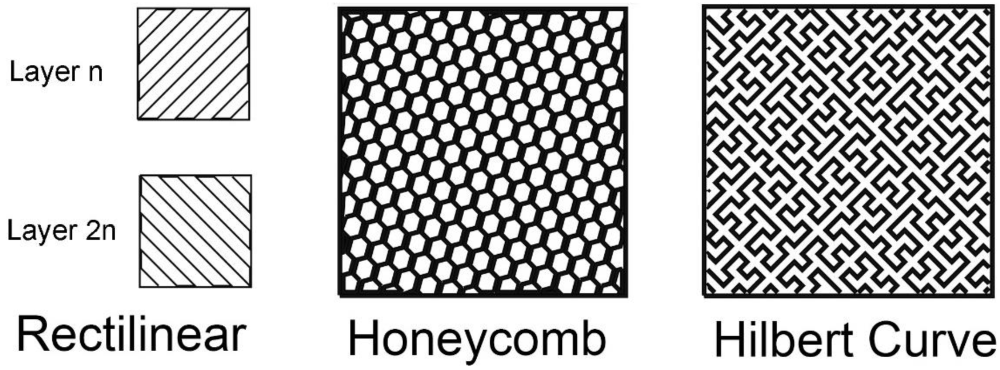

Figure 2.2: The three infill patterns at 30% density. The rectilinear pattern alternates every other layer.

For FDM processes, the infill density, raster angle, layer thickness [11] and part orientation are among the most important process parameters affecting the mechanical strength of a part. Strength and anisotropy are significant problems for thermoplastics parts produced by FDM processes and make properties of finished parts under complex loading difficult to predict [12]. The ultimate tensile strength of acrylonitrile-butadiene-styrene (ABS) parts has been shown to vary over an order of magnitude depending on the raster angle [13]. Layer thickness has been shown to be inversely related to tensile strength [14]. In compression, fully dense ABS specimens were shown to have the highest yield stress, but honeycomb infill patterns have the highest strength-to-weight ratio [15].

Compared to FDM, relatively little is known about the how the process parameters affect the mechanical properties of 3D printed elastomers. Duoss *et al.* [16] was the first to report 3D printing of elastomeric foams using simple cubic (SC, also commonly known as rectilinear) and face-centered tetragonal (FCT) patterns. Both patterns exhibited negative stiffness under simple shear deformation. Under uniaxial compression, the printed foams were found to undergo buckling due to deformation of the column-like cross-over points of printed strands. Later work described the tunability of the SC and FCT patterns under compression by changing the spacing of the strands [17]. Shih and Plott [18] also demonstrated the feasibility of RTV elastomers as printing materials by printing simple line geometries and implemented a model to predict the flow rate of a function of pressure. In a later work, Putra, Shih and Plott [19] characterized solid printed RTV specimens in equibiaxial tension and determined that voids in thin specimens affect strain distribution while the compression of many layers in thick specimens eliminated such voids. Qiu *et al.* [20] demonstrated inks with tunable Young's moduli from 10-50 kPa to mimic human tissue by addition of a silicone grease to an RTV silicone and successfully printed model organs from MRI data for surgical rehearsal. These previous studies have been limited to solid or small parts with simple geometries, and the effect of infill geometry and density have not been systematically studied in the literature for printed elastomers.

In this work, we expand on the previous foundations by characterizing the tensile properties of rectilinear/simple cubic patterns as a function of infill density and reporting compressive properties of two new patterns, a space-filling Hilbert curve and a honeycomb pattern. This work also details how the mechanical properties can be tuned simply by changing the infill density or pattern, which provides designers a means to tune the response and properties of a part without changing the material or part geometry.

3. Experimental

A modified H-style XY gantry, utilizing NEMA-23 stepper motors and lead-screw driven Z platen, is used as the mechanical basis for our printer, though any platform capable of three axis movement is also suitable. A RAMPS 1.4 board is used as a peripheral breakout board from the Arduino ATMega 2560 motherboard. The stepper driver and carriers (TI DRV8825, Pololu Robotics and Electronics) are capable of 1/32 microstepping, and the XYZ axes have 135 ,105 and 634- steps per millimeter, respectively. For printing, a 30 mL syringe (Nordson EFD, Inc) is used as the material reservoir and a tapered nozzle with orifice size of 410 µm (Nordson EFD, Inc) is attached to the syringe.

The pneumatic system, as show in Figure 3.1, is built from a 3/2 solenoid (ARO P251SS024-D, Grainger) triggered using a signal from the Arduino. All other components were assembled using 6 mm OD pneumatic tubing rated at 145 psi with push-to-connect fittings. The pressure is tuned manually by using the dispense regulator.

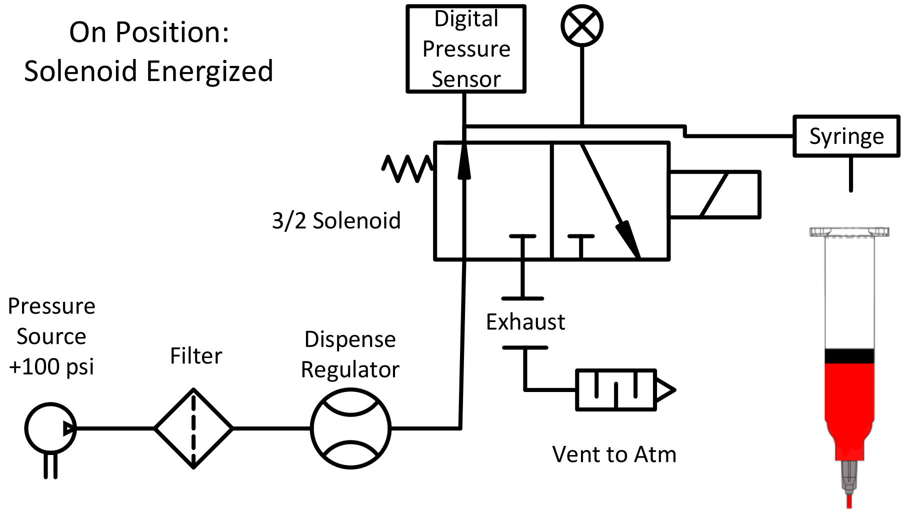

Figure 3.1: Schematic of pneumatic dispense system.

Since a 24V solenoid was chosen, it cannot be actuated directly from the RAMPS board. Rather, the interface circuit in Figure 3.2 is used. It is important to note that even if a 12V solenoid is used directly with the RAMPS board (such as the heated stage or fan pins), a reverse-biased diode is still necessary across the coil leads, since it is an inductive load.

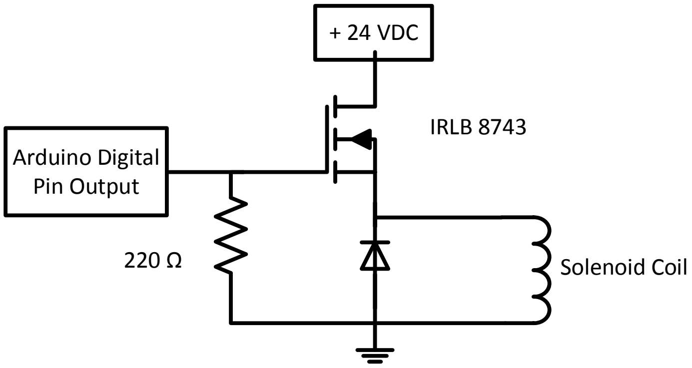

Figure 3.2: Interface circuit to actuate solenoid using Arduino low-voltage outputs

Pressure-time data is collected with a digital pressure sensor (QPSH-AN-42, Automation Direct) and an Arduino Mega 2560. A MATLAB script is triggered to begin collection by a digital output on the pressure sensor as shown in Figure 3.3. Data is stored in an array by reading a voltage across an analog input pin and a resistor to convert the standard 4-20 mA analog industrial control output into a 0-4.4 V signal.

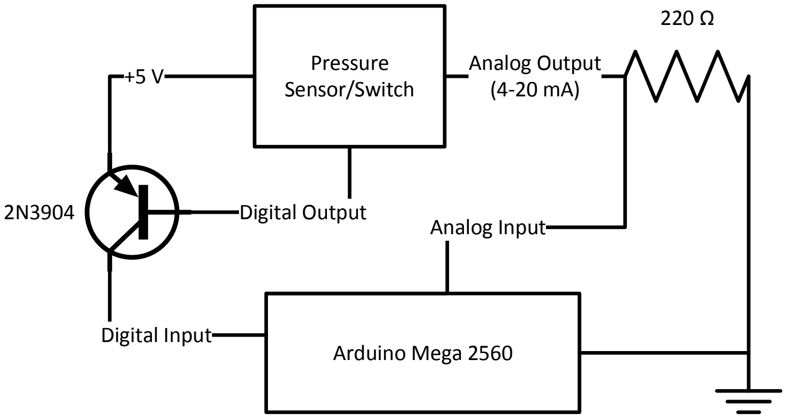

Figure 3.3: Pressure-time data collection circuit to trigger collection and log data

Marlin firmware is used on the host microcontroller, and Repetier/Slic3r is used on a host desktop to generate and send g-code. Many varieties of firmware and software are available for 3D printing, but they are specifically optimized for mechanical extrusion of thermoplastic filaments. 3D printers and CNC machinery use a general programming system called G-Code for control. Motion planning is done on-the-fly in the microcontroller, only raw coordinates, feedrates and machine codes are sent to the microcontroller. One problem familiar to computer science is the precedence of commands. Since path planning is done on-the-fly, some commands are stored in the buffer until executed. However, solenoid actuation commands must be executed sequentially. Thus, it is necessary to use interrupted-based M-codes to actuate the solenoid. In the version of Marlin used in this work, the auxiliary pin commands (i.e. Pxx Sxx, where P references the pin number and S the state of the pin). The state is pulse-width modulated on a the 8-bit architecture, meaning that values range from 0-255 (2^8). A post-slicing script is used to replace firmware retraction and priming commands (G10 and G11, respectively) with commands to actuate the solenoid through use of a digital pin on the Arduino (M42 Pnn Snnn).

The volumetric flow rate is calibrated empirically using a timed cycle. A commercially available a single-component acetoxy-cure RTV silicone (General Electric All-Purpose Silicone, Momentive Performance Materials) was used as the feedstock and an 87 wt% glycerol/13% water solution was used to as a standard of comparison. The silicone cures upon exposure to atmospheric moisture, has a 30-minute tack-free time and 24-hour through-cure. The cycle is set for 5 seconds to ensure that the amount of extrudate is much greater than the minimum resolution of the balance used for weighing (~0.001 g) at the lowest ranges of pressures used. The results of the calibration are shown in Figure 3.4.

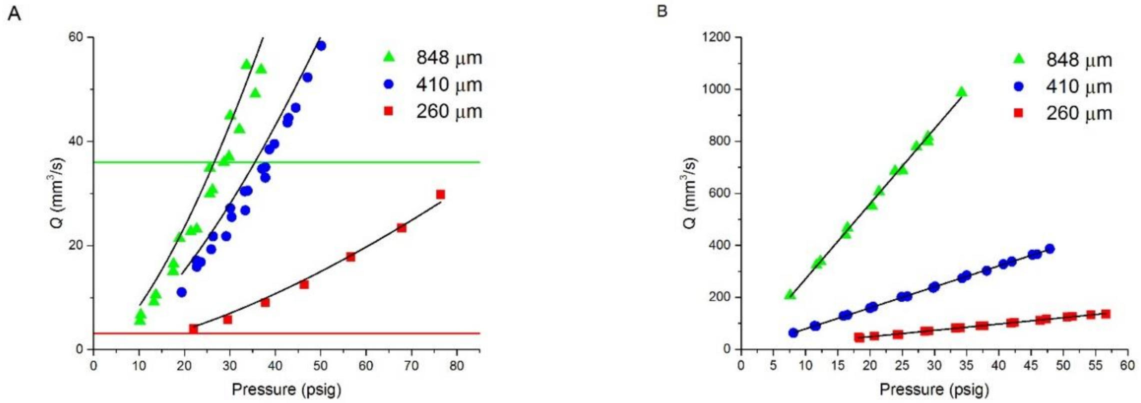

Figure 3.4: Volumetric flow rate as a function of pressure for A) Silicone B) Glycerol solution.

The solenoid has a finite time for engagement due to the energization of the coil which must considered. Another confounding factor is the time to reach the fluid yield stress and pressurization of the syringe. This can be calibrated empirically using a digital pressure sensor to determine the time where a steady-state pressure is achieved. Compensation for the finite time between actuation and steady-state extrusion is achieved through a delay command (G42 Pxxx), where P refers to the delay time in milliseconds. Pressure-time data for a 500 ms dispense cycle in Figure 3.5 shows the rate of pressure increase and decrease for a given target or set pressure. The time taken to reach the set pressure and thus steady volumetric flow rate is approximately 150 ms. One interesting feature is that the decrease for the 14.8 and 24.3 psi experiments does not match the 34.9 psi experiment. This is attributed to the timing of data collection and the response of the sensor, which misses points at the end of the two curves. Further optimization of the program is needed to capture these points.

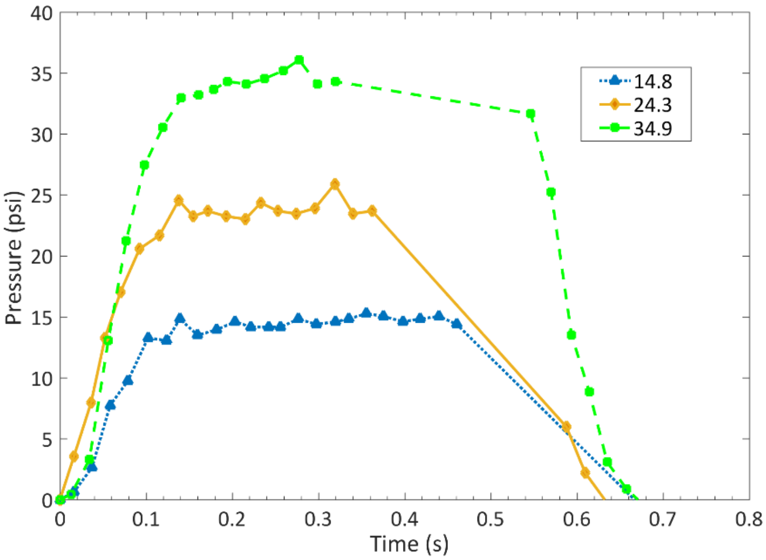

Figure 3.5: Pressure vs. time data for a 500 ms pulse at three different pressure setpoints.

Although the rate of pressure increase is fast, approximately 358 psi/s, a delay to allow material to begin flowing before the printhead moves is necessary to establish adhesion to the previous layer. Failure to incorporate a delay results in the defect shown in Figure 3.6.

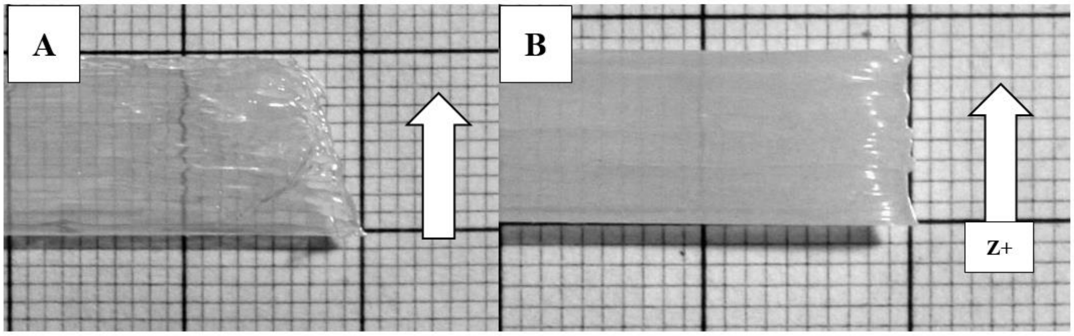

Figure 3.6: Effect of delay on printed single-width lines showing A) scalloped and poorly defined edge with no delay B) well-defined sharp edge with 150 ms delay

Test prints were also performed to check dimensional accuracy and slice height accuracy. A cross-section of the 100% rectilinear infill test sample printed with a 410 µm diameter nozzle is shown in Figure 3.7. This shows that the structure contains few macroscopic defects except for very small voids and is dimensionally accurate when accounting for shrinkage and fluctuations in the pressure. The layer height matches that of the software slicer setting (300 μm). Vertical streaks are an artifact of the razor blade used to cut the sample.

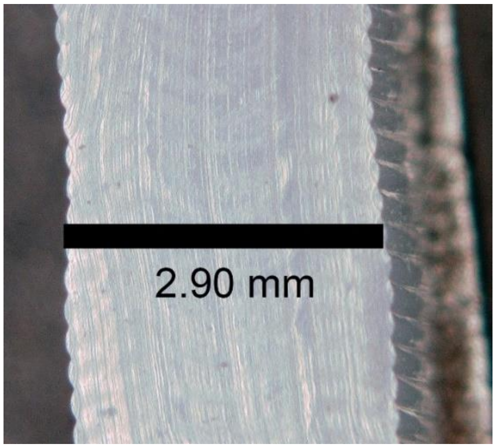

Figure 3.7: Cross-sectional image of printed structures cut with razor to show internal features and verify dimensional accuracy of the 3.00 mm nominal width. Printing parameters are v=60 mm/s, P=30.8±1 psi, d_o= 410 μm.

The relative density (defined as the density of the printed part over the density of the bulk material) is important for foams and other materials with inclusions. 40x40x10 mm rectangular prisms were printed to determine the relative density. Figure 3.8 shows the connection between the measured relative density and the infill density specified in the slicing program. Ideally, there would a one-to-one relationship between these two properties once the effect of the solid polymer (i.e. the perimeters and top/bottom shells) is accounted for. However, this is not the case; density provided by the slicing software do not agree. Only the honeycomb pattern shows a linear relation between relative density and the software infill density. For a macroscopic part, the number of top/bottom shells and perimeters also factors into the relative density.

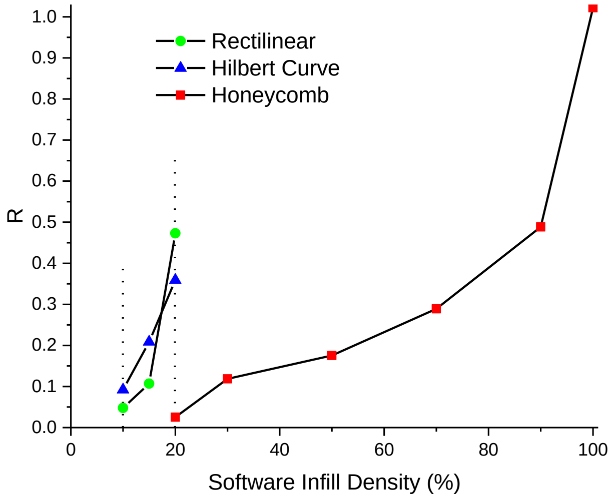

Figure 3.8: Infill density selected in software versus experimental relative density of compression samples (R). Vertical dash lines indicated printable range for material and setup using honeycomb and Hilbert Curve geometry.

4. Mechanical Characterization

4.1 Rheology

Rheological characterization of the uncured silicone was performed at 25 °C using an AR-G2 rheometer (TA Instruments) with a 40 mm parallel plate geometry. To negate effects of slip, 320-grit adhesive backed sandpaper was applied to both the upper and lower geometries. Flow curves were collected by logarithmically increasing the shear rate from 0.01- 200 s-1 and monitoring the shear stress. Storage (G') and loss (G'') moduli were measured using an oscillation frequency of 1 Hz and controlling the oscillatory stress from 1-400 Pa.

The results of the oscillatory stress sweep are shown in Figure 4.1. The storage modulus, G', and loss modulus, G", are constant until a stress of ~100 Pa at which point both begin to drop. A high storage modulus in the plateau region (10^4 Pa) compared to the loss modulus in the same region (10^3 Pa) indicates solid-like behavior at low stresses, while at higher stresses the viscous behavior dominates as *G''>G'*. The oscillatory stress sweep shows well-defined yield stress behavior, with a yield stress, τ_y, of ~400 Pa as defined by the crossover of *G'* and *G'*. These characteristics are typical for sealants and desirable for both sealant and printing materials because

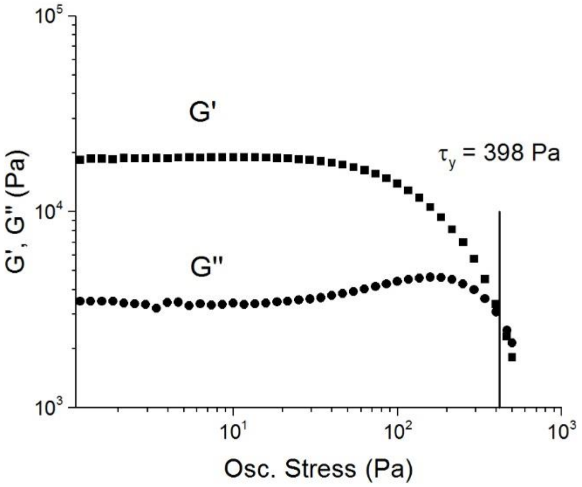

Figure 4.1: Storage and loss modulus (G' and G", respectively) gathered in an oscillatory stress sweep for the silicone feedstock. The yield stress, τ_y, is noted.

a high value of *G'* and solid-like behavior negate sag at low stresses such as those experience after application.

Shear rheology data measured using shear rate ramps results show strong shear thinning as shown in Figure 4.2.

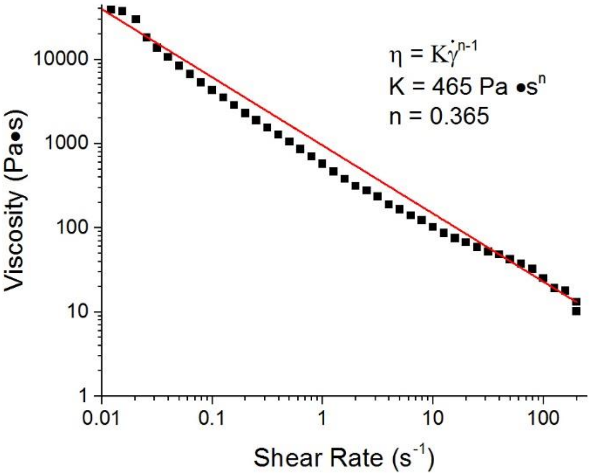

Figure 4.2: Shear rate ramp results. Line indicates fit to Equation 1.

The viscosity, η, drop with shear rate follows a power-law model:

$$\eta = K\dot{\gamma}^{n-1} \tag{1}$$

where *K* is the consistency index and *n* is the power law index. From data analysis, *K* = 465 Pa·s^n and *n* = 0.365. This behavior is fortuitous for 3D printing because shear thinning behavior allows the material to flow readily with application of reasonable pressures and the high viscosity at low shear rates imparts dimensional stability after extrusion while curing takes place. At very high shear rates (>200 s^{-1}), the flow becomes unstable due to edge fracture, and the material exits the geometry gap leading to the drop-off shown.

4.2 Process Limitations

The process has two separate factors that ultimately limit the throughput: the machine and the material. The machine is limited by the maximum velocity that the printhead can be moved before causing excessive vibration due to rapid deceleration and the maximum pressure achievable. The material is limited in the maximum viscosity that can be extruded with reasonable pressures.

For the machine used in this work, the maximum safe velocity was determined to be 100 mm/s and the safe working pressure of the syringe and fittings is 90 psig (~620 kPa). Using these values, a maximum volumetric flow rate can be determined when the cross-sectional area of the extruded silicone is known. This cross-sectional area changes as a function of the slice height to orifice diameter (h/d_o). When $h/d_o=1$, the extrudate cross section is circular, which is not ideal for printing because there is only a small surface of contact at the tangent point of adjacent extrudate. In this work, the h/d_o ratio was chosen to be ~0.7, a value common in FDM printing that provides a fast printing speed (more thickness per layer) while maintaining a roughly rectangular cross-section. Due to conservation of mass and assumption of incompressibility, Q, the volumetric flow rate out of the nozzle determined experimentally as a function of pressure can be equated to the flow rate of the printed polymer line (c):

$$Q(P) = Q_{line} = h \cdot d_o \cdot v \qquad (2)$$

Therefore, assuming the maximum velocity of 100 mm/s and the values for (410 µm) and h (0.7*410 µm), we find that the maximum output is 11.7 mm^3/s. According to the data in Figure S1 for RTV silicone, this value is on the low end of the measured calibration data. This result implies that the process speed is limited by the maximum speed achievable with the printer and not the pneumatic system.

The second factor is the material rheology, which could limit the volumetric throughput. If the viscosity is too high, flow rates are limited by the available maximum pressures. The syringe can be modelled as a tapered tube with geometrical constants previously shown in Figure 1B. The effect of friction on the barrel of the syringe is small (i.e. $P_1 \ll P_3$) compared to shear flow through the nozzle and is neglected. The pressure drop into the die is also negligible (i.e. $P_2 \ll P_3$). Using the power-law fit from the shear ramp experiments (Figure 4), where K= 465 $Pa \cdot s^n$ and n=0.635, the maximum flow rate at 90 psig from the nozzle can be derived using the equation for shear flow in a slightly tapered tube using *Equation 3* [21]:

$$Q = \frac{\pi d_o^3}{\frac{8}{n}+24}\left(\frac{P d_o}{4KL}\right)\left(\frac{3n(\lambda-1)}{1-\lambda^{-3n}}\right)^{\frac{1}{n}} \tag{3}$$

where $\lambda = d_o/d$. Polymer solutions and melts typically have a shear thinning index (n) value between 0.3 and 0.7, so taking $n=0.5$ as an average value allows the maximum value of K to be solved as $212 \cdot 10^3$ Pa·s^n, which is approximately three orders of magnitude more viscous than the polymer used in this work. This concurs with the analysis above that the speed of the machine ultimately limits the throughput and even higher viscosity polymers can be used with the printer described in this work.

4.3 Preparation of Parts for Mechanical Tests

Four sample types are used in this study: compression, tensile, cast and solid. Excluding cast samples, all printed samples were prepared using the following procedure. First, the CAD model is imported into the slicer software and sliced at 300 µm slice height with a 45° infill angle relative to the XY plane for rectilinear infills. A printhead velocity of 60 mm/s was chosen, which corresponds to a pressure of 30.8 psi based on results of the calibration experiment and cross-sectional area of the path. Generated g-code is run through a post-processing script to include commands that actuate the solenoid and add a 100 ms delay between the actuation of the solenoid and motion of the printhead. The delay accounts for the time between solenoid energization and material extrusion. The pressure was set using the regulator to 30.8±1 psi before attaching the syringe and purging the nozzle. A 2 mm thick glass plate was secured to the build platform before commencing the print. After completion, curing was carried out at a temperature of 23 °C and a relative humidity ranging from 30-50% for a minimum of 24 hours. The specimens are then delaminated from the build plate using a razor blade.

Square specimens (40 x 40 x 10 mm) for compression testing were printed using the previously outlined parameters with two top and bottom shells for mechanical stability and two outer perimeters (i.e. outer walls). The height was chosen to sample at least 50 layers and minimize size-dependent effects. The width was chosen to be larger than the compression fixture, which minimizes the effects of the solid perimeters and maximize the mechanical response of the infill.

Modified ISO37 Type 1A specimens were printed for tensile testing. These samples have two perimeters (walls) and no top or bottom shells to maximize the contribution of infill to mechanical response. The tensile test study was limited specimens prepares with the rectilinear infill pattern only; the small size of the gauge region did not allow the 2D honeycomb and Hilbert curve patterns to be produced fully. Further, specimens were designed so that the grip regions were only perimeters, then could be made solid by a post-printing step. This multi-step method was implemented to improve repeatability of tensile samples. First, specimens were printed with the designed pattern in the gauge but only walls in the grip region of the dumbbell. The printed specimens were cured for 24 hours, then the grip region was manually filled with silicone and levelled with a spatula. After another 24 hours, the samples were delaminated from the glass build surface using a razor, flipped over and any remaining voids were filled. Samples were then cured another 24 hours before testing. This procedure guarantees the sample is solid at both ends, which ensures that the state of stress is the same in this region regardless of the infill density in the gauge region. For the complete preparation procedure and geometry, see Figure 4.3.

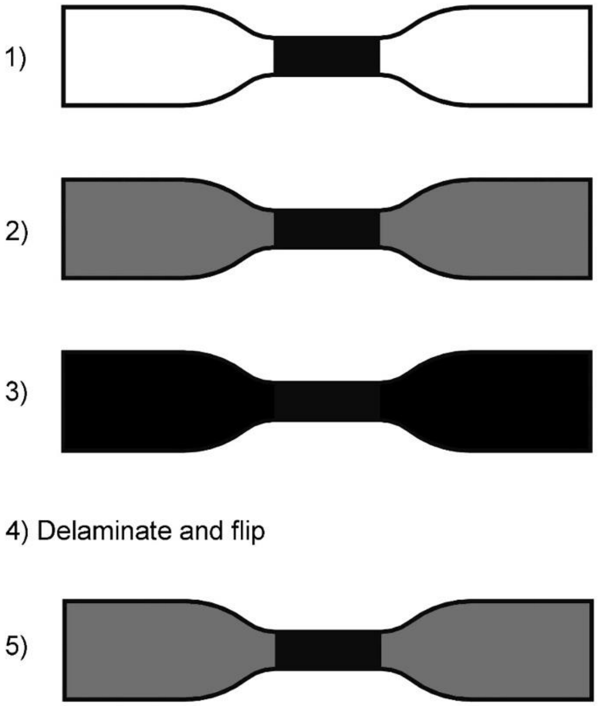

Figure 4.3: Tensile sample preparation process. 1) Specimens are printed with only walls in the grip region and then cured for 24 hours. 2) Liquid silicone (gray) is manually extruded into the void region and is levelled using a spatula then allowed to cure 4) After 24 hours, the entire specimen is delaminated from the glass build surface using a razor blade. 5) The sample is flipped over and any remaining voids are manually filled with silicone and levelled off with a spatula.

This method also dramatically decreased the occurrence of failure outside the gauge region, which is common in elastomers and invalidates the results of the test. Adhesion between the uncured and cured interface was excellent and failure at the interface was rare when the filling and levelling procedure was performed carefully. An experimental relative infill density, R, of a section of the gauge region was found using the method described in the previous chapter.

A sample 10 x 3 x 10 mm was printed with 100% rectilinear infill to verify dimension accuracy of the widths and layer heights. The sample was cross-sectioned and imaged with an optical microscope. Cast samples for comparison to printed specimens were prepared by extruding silicone into 3D printed negative mold of the tensile bar geometry and drawing a metal bar across the top surface to level it and compress the silicone to fill the mold. Tensile testing was performed at 23 °C using an Instron 5966 universal testing system equipped with a 500 N load cell and pneumatic grips set to a pressure of 10 psi. Before commencing crosshead motion, a 1 N pre-load was applied to remove slack. A crosshead extension rate of 50 mm/min and an AutoX750 extensometer were used to measure strain at an initial gauge length of 20 mm. After testing, digital scans were taken for each set of samples using an Epson WF-2530 flatbed scanner at a resolution of 1200 dpi (47.24 pixels/mm) to determine the cross-sectional areas near the fracture region and sample widths. ImageJ was used to manually trace the entire outer perimeter of the sample to determine the area.

Compression tests were performed at 23 °C using an RSA-G2 rheometer (TA Instruments) with a 25 mm diameter stainless steel parallel disc fixture at a compression rate of 20 µm/s to a strain of 75% or until the 3 kgf max load of the instrument was reached. To the minimize the Mullins effect [22] (strain softening), the sample was precycled three times to the maximum stress then released before taking the measurement. The sample was oriented such that the infill pattern (positive z direction of sample) is parallel to the compression axis and the circular plates were centered on the specimen such that the solid perimeters of the 3D printed blocks did not contribute significantly to the response. Dynamic mechanical analysis (DMA) was carried using the same geometry by pre-application of 12.5% strain at an oscillation frequency of 1 Hz and strain amplitude from 10^{-1} to 10^{1}.

4.4 Compression Test Results and Discussion

Compressive stress-strain curves for rectilinear patterns are shown in Figure 4.4. The curves are labeled with the relative density, R, determined experimentally. With low density infills (<30%) and low R values (≤ 0.119), there are three regions identifiable. At strains <0.1, there is a linear elastic region until a plateau is reached. When the plateau is reached, buckling of the internal structure occurs. Finally, at compressive strains >0.4, densification occurs, where the internal structure is fully compress and the behavior mimics that of the bulk material. Note that air inside the specimen can escape through gaps in the top shells. For higher relative densities (higher infills), no buckling occurs in the range of stresses tested. A linear fit of the linear elastic region (neglecting the initial “toe” regions due to sample slack [23]) shows a monotonic trend of the slope (i.e. modulus), increasing with infill density is apparent as shown in Table 4.1.

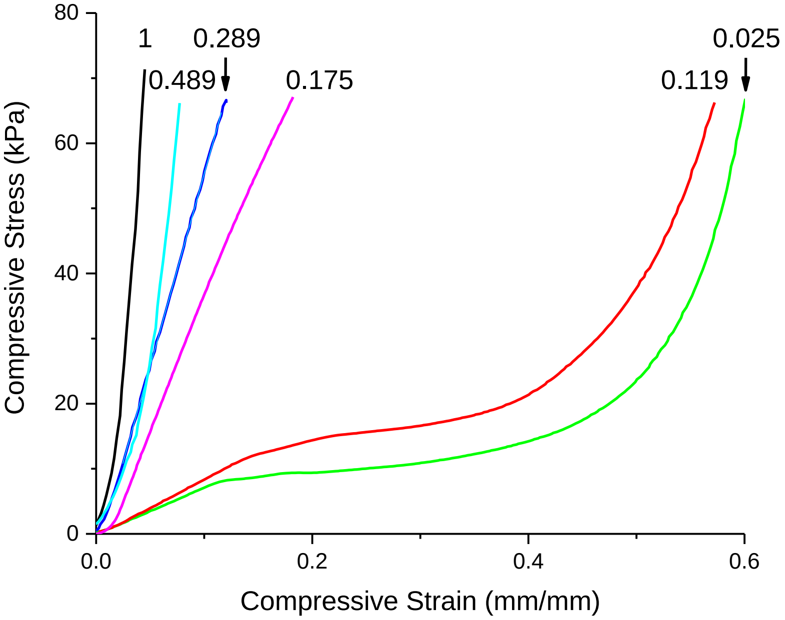

Figure 4.4: Stress-strain curves for 3D printed silicone samples rectilinear infill pattern as a function of relative density, R, which increases with infill density.

Table 4.1: Summary compressive modulus data as a function of relative density for fitting in linear elastic region.

Pattern	R	Modulus (kPa)
Rectilinear	0.025	72
	0.119	88
	0.175	420
	0.289	590
	0.489	1100
	1	2000
Honeycomb	0.092	120
	0.359	400
Hilbert Curve	0.048	170
	0.107	170
	0.473	430

The effect of infill on the modulus can be understood based on the geometry of the infill region. Samples with infill densities less than 100% fully-dense infill can be described in terms of an effective cross-sectional area in the central portion. For samples in compression, this cross-section is defined by the area occupied by the infill strands. A fully dense sample has an effective area equaling that of the entire platen. The effective area for rectilinear compression samples versus relative density is shown in Figure 4.5. The data shows good correlation between the effective area and relative density. The intersection of the fit line and actual platen area at R=1 occurs near a value of 491 mm^2, which is expected in the case of fully-dense samples. The y-intercept near 0 is also expected since a sample with a R=0 there will be no material bearing the load.

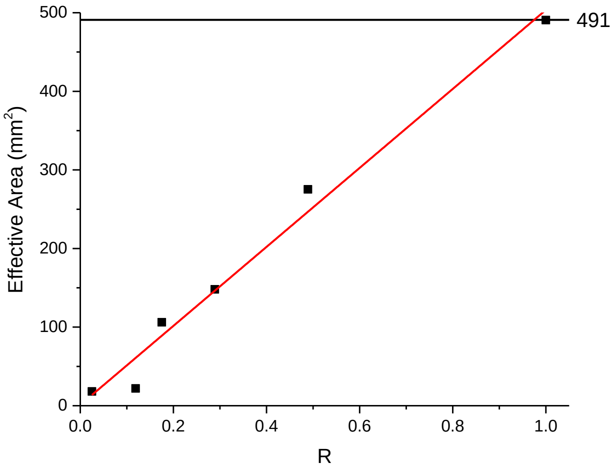

Figure 4.5: Effective compression area versus relative density (R). Horizontal line at y=491 mm^2 represents the total area of the platen with 25 mm diameter. Red line indicates a linear fit.

For the Hilbert curve and 2D honeycomb patterns, the range of useful patterns is more limited. They also display buckling behavior at low densities as seen in Figure 4.6, before undergoing densification. The Hilbert curve pattern displays a peak before buckling that is characteristic of "snap-through" buckling, where the stiffness becomes negative as the walls of the infill collapse and stress is relieved through lateral deflection [24]. When a critical stress is reached, buckling spontaneously occurs and then decays into the plateau region before densification. This is distinct from the buckling observed in the honeycomb or rectilinear patterns. Upon unloading, hysteresis is observed due to mechanical energy dissipated as vibrations when buckling occurs as shown in Figure 4.6. Additionally, it has been shown dissipation is independent of loading rate given the loading frequency is lower than the frequency of vibration [25].

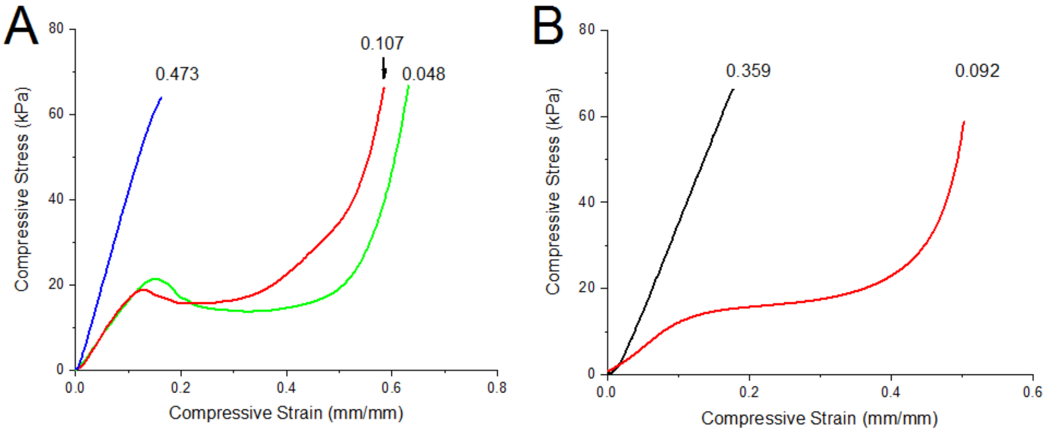

Figure 4.6: Stress-strain curves of A) Hilbert curve and B) honeycomb infill as a function of relative density.

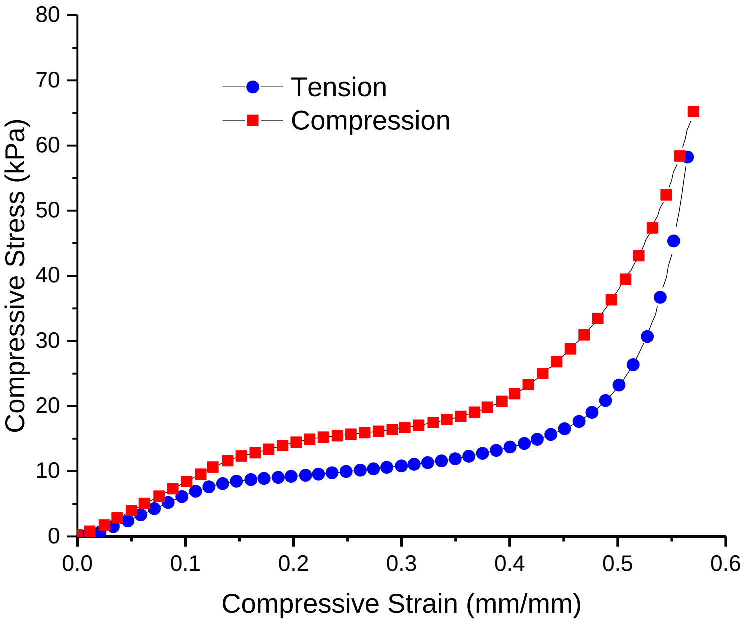

Figure 4.7: Hysteresis loop for a 30% rectilinear infill sample.

The dynamic storage moduli for all samples under compression is summarized in Figure 4.8. The data shows good correlation of the modulus with the density, indicating that control over the modulus is readily achievable.

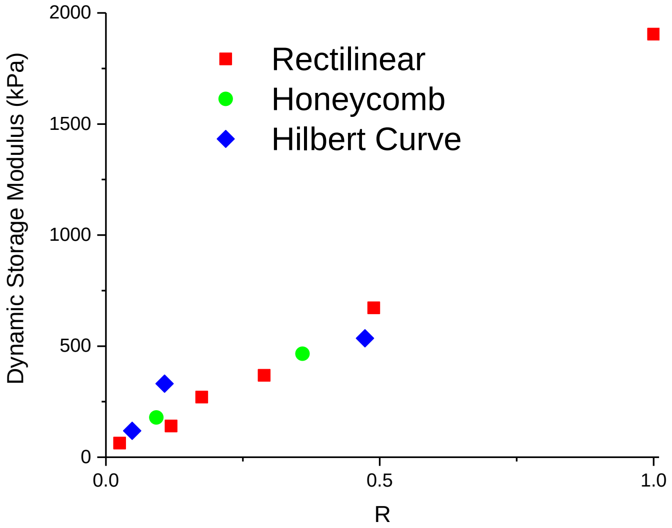

Figure 4.8*:* Compressive dynamic storage modulus (*G'*) vs. relative density for the three patterns.

4.5 Tensile Test Results and Discussion

It is important to accurately determine the cross-sectional area of each tensile test specimen for data analysis. The nominal cross-sectional area of the CAD file is 40 mm^2 and digital scans show 50% and 70% are the most dimensionally accurate. At low infill densities, the area is slightly less than the CAD dimensions due to sag of the individual strands of material. The digital scans show that outer perimeter walls are much thicker than expected and this effect increases with infill density. For small areas, such as the gauge region of a tensile sample, this effect is difficult to avoid due to a constant pressure providing a constant volumetric flow rate while the printhead velocity changes during abrupt changes in direction. The effect can potentially be minimized by increasing acceleration or decreasing the printhead velocity. Dynamic pressure regulation could enable higher speed printing while maintaining dimensional accuracy.

Tensile test data for specimens prepared with rectilinear infill is shown in Figure 3.17. The silicone elastomer shows nonlinear elastic behavior throughout the entire stress-strain curve.

The sudden drop in stress indicates that the sample has ruptured. Silicone elastomers display drastically different stress-strain behavior than typical thermoplastics used in 3D printing. Polymers like polylactic acid (PLA) display reversible elastic strain up to 1% [26] and brittle fracture at failure. Natural rubbers behave linearly up to strains of approximately 10% followed by non-linearity up to failure [27]. No permanent tensile set is observed after rupture, which implies that plastic deformation is negligible. Failure occurs in purely elastic manner. Interestingly, the stress-strain curves for the R=0.75 and 0.81 (infill percentages of 50 and 70%, respectively) curves almost overlap even after replication. It is apparent that the slicer is less sensitive to incremental changes in the 50-90% region than the 20-50% region. Another interesting feature is the large difference between the R=0.81 and 0.83 samples. Despite the small change in relative density, there is a noticeable difference in the modulus. One possible explanation of this difference is the further development of solid regions without infill gaps in the R=0.83 sample, which would increase the modulus. This is supported by the digital scans. The overlap of the R=0.75 and 0.81 samples also supports this conclusion; despite the difference in relative density, the wall thickness is similar. Overall, wall and shell thickness have a noticeably larger effect on the modulus than the absolute value of infill density.

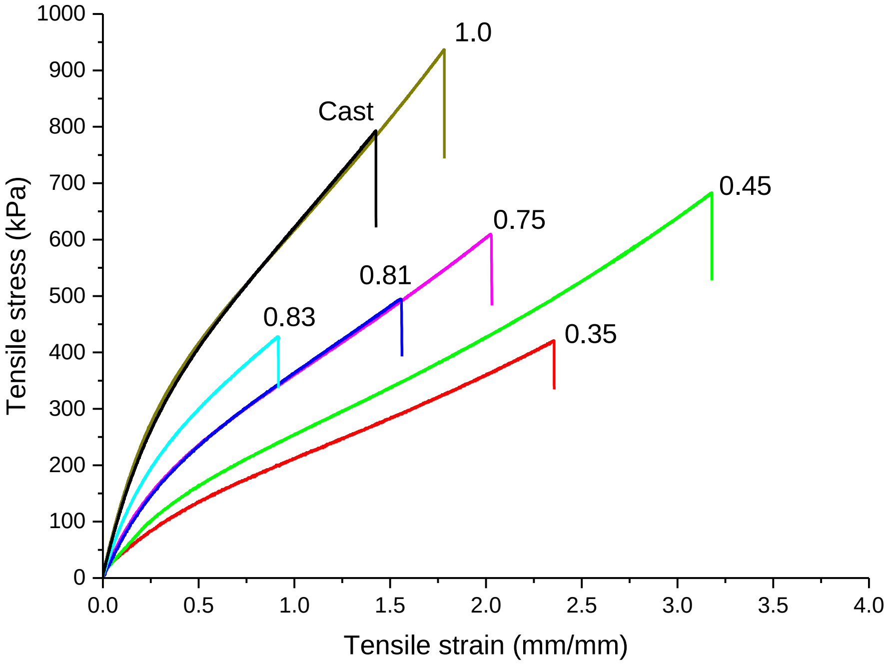

Figure 4.9: Representative stress-strain curves of silicone specimens prepared with rectilinear infill at varying infill density; labels are the estimated relative density (see Table 4.1). The sudden drop in stress indicates the sample has ruptured.

The effective Young's modulus was determined by a linear fit at strains from 0 to 0.2; see Figure 4.10 and Table 4.2. Data for cast and 100% dense printed samples show good agreement and capability of the process to print 100% dense parts without diminishing mechanical strength.

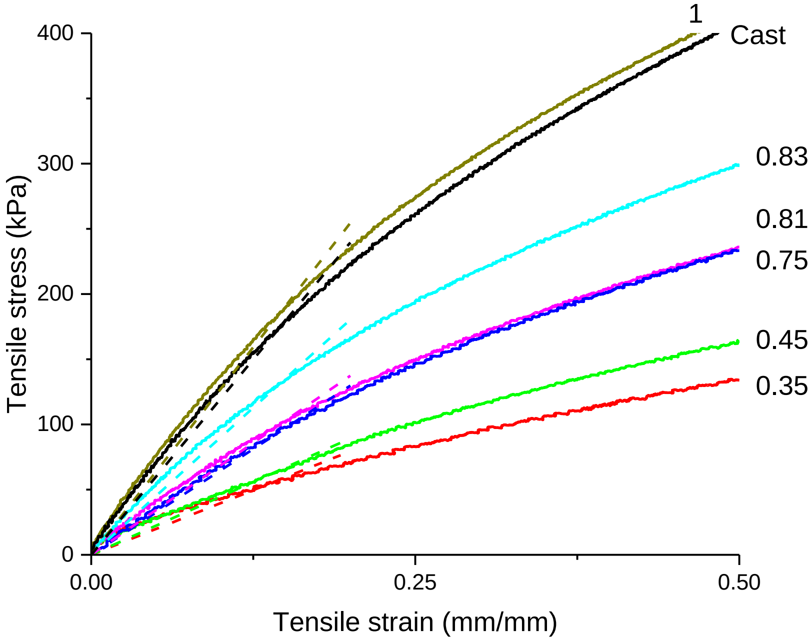

Figure 4.10: Representative small-strain (<0.5) stress-strain curves for rectilinear infill samples. Dashed lines indicate a linear fit for the apparent modulus at strains from 0-0.2.

Table 4.2: Summary of apparent Young's modulus as a function of relative density for strain values from 0-0.2.

R	Apparent Young's Modulus (kPa)
0.35	310 ± 20
0.45	380 ± 50
0.75	620 ± 30
0.81	630 ± 30
0.83	820 ± 30
1.0	1150 ± 30
Cast	1110 ± 40

High variation is observed in the strain at failure and ultimate tensile strength, but overall the plot shows the expected trend of increasing mechanical strength with increasing infill density as summarized in Figure 4.11. Other reports on mechanical properties of elastomers describe similar variation due to the strain distribution outside of the gauge region of the sample [28].

Another proposed reason for the variability in 3D printed samples is stress concentrations near the fillet of the sample due to the discretization that happens in STL files [29], which can also lead to failure outside the gauge region. However, in our data set only failures inside the gauge region are reported. We expect stress concentration in gauge region due to the infill structure and hence variability in the failure stress and train at break may be related to this effect.

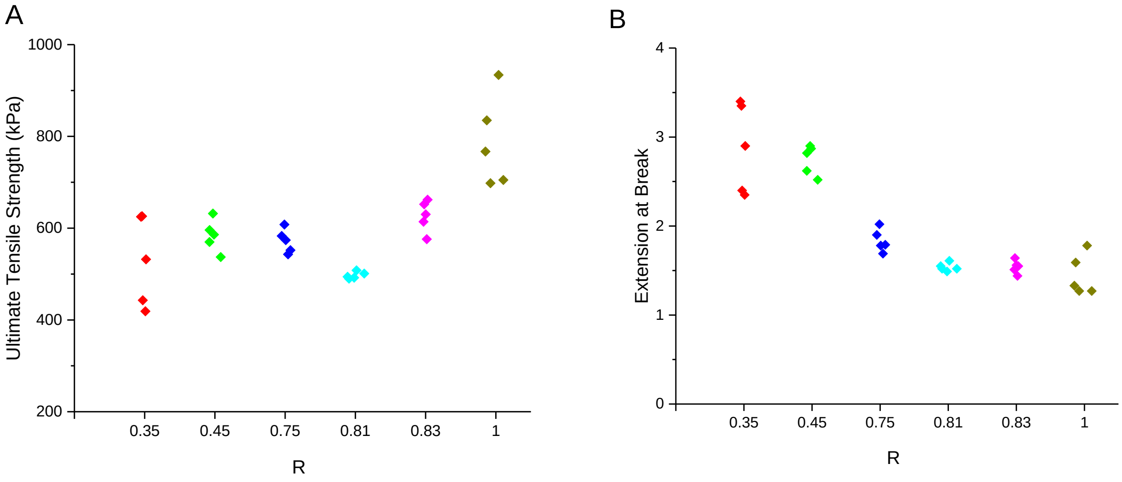

Figure 4.11: Summary of tensile test data for rectilinear infill samples. A) Average extension at break vs. relative density. B) Ultimate tensile strength vs. relative density.

The decrease in extension at break with increasing density could be also be due to the presence of the internal structure. In the case of a fully dense sample, stress concentrates at microscopic defects inherent to the printing process. At these concentrated areas, rupture occurs when stresses exceed the strength of the crosslinked network. In a specimen with less than 100% infill, it is possible for the macroscopic printed strands to rotate in the direction of applied stress to distribute the load before the sample fails. In this case, it would be expected as the number of strands increases (i.e. an increase in relative density and infill percentage), there would be more junction elements to rotate and thus a higher extension could be reached before any single one ruptures.

5. Conclusions

Silicone 3D printing is a promising method for facile fabrication of elastomeric parts. A custom-built printer was built and characterized. The effect of infill density and infill pattern on the mechanical response of 3D printed silicone elastomers was investigated. An important consideration is calibrating the slicing software infill density to the actual relative density. Printed specimens with a range of infill densities and several infill geometries were tested under uniaxial tension and compression. In tension, the stress-strain behavior is non-linear over the entire curve. Ultimate tensile strength is relatively unaffected by infill density over a range of relative densities from 0.35 to 1.0, while extension at break decreases with increasing infill density. The apparent Young's modulus was determined in the small-strain limit and is tunable from 310-1150 kPa by adjusting the infill density. Tensile strength of fully-dense printed samples (1150±30 kPa) is comparable to that of the bulk cast samples (1150±40 kPa). In compression, the stress-strain properties of three different infill patterns over a range of infill densities were determined. The specimens exhibited stress-strain behavior typical of foams—a linear elastic region with a modulus dependent on infill density, followed by a buckling plateau region and densification at high strains. Negative stiffness due to snap-through buckling was observed. Results for both tension and compression tests show the tunability of mechanical response achievable through changing the software infill density.

Bibliography

[1] I. Gibson, D.W. Rosen, B. Stucker, Additive Manufacturing Technologies: Rapid Prototyping to Direct Digital Manufacturing, Springer, New York, NY, 2010.

[2] Plastics Today, Additive manufacturing market forecast to reach $23.3 billion by 2026, Plast. Today. (2019). https://www.plasticstoday.com/medical/additive-manufacturing-market-forecast-reach-233-billion-2026/131939267760466 (accessed February 9, 2019).

[3] E. Peng, D. Zhang, J. Ding, Ceramic Robocasting: Recent Achievements, Potential, and Future Developments, Adv. Mater. 30 (2018). doi:https://doi.org/10.1002/adma.201802404.

[4] J.A. Lewis, Direct ink writing of 3D functional materials, Adv. Funct. Mater. 16 (2006) 2193–2204. doi:10.1002/adfm.200600434.

[5] R. Jones, P. Haufe, E. Sells, P. Iravani, V. Olliver, C. Palmer, A. Bowyer, RepRap - The Replicating Rapid Prototyper, Robotica. 29 (2011) 177–191.

[6] J. Mark, H. Allcock, R. West, Inorganic Polymers, Prentice Hall, 1992.

[7] J. Cai, 4D Printing of Soft Robotic Facial Muscles, J. Chem. Inf. Model. 53 (2013) 1689–1699.

[8] Drotman D., S. Jadhav, M. Karimi, P. DeZonia, M.T. Tolley, 3D Printed Soft Actuators for a Legged Robot Capable of Navigating Unstructured Terrain, IEEE Int. Conf. Robot. Autom. (2017).

[9] S.-Z. Guo, K. Qiu, F. Meng, S.H. Park, M.C. McAlpine, 3D Printed Stretchable Tactile Sensors, Adv. Mater. (2017) 1701218. doi:10.1002/adma.201701218.

[10] J.T. Muth, D.M. Vogt, R.L. Truby, Y. Mengüç, D.B. Kolesky, R.J. Wood, J. a. Lewis, Embedded 3D printing of strain sensors within highly stretchable elastomers, Adv. Mater. (2014) 6307–6312. doi:10.1002/adma.201400334.

[11] T. Letcher, B. Rankouhi, S. Javadpour, Experimental Study of Mechanical Properties of Additively Manufactured ABS Plastic as a Function of Layer Parameters, Vol. 2A Adv.

Manuf. (2015) V02AT02A018. doi:10.1115/IMECE2015-52634.

[12] J.R.C. Dizon, A. Espera, Q. Chen, R. Advincula, Mechanical characterization of 3D-printed polymers, Addit. Manuf. 20 (2018) 44–67.

[13] B. Rankouhi, S. Javadpour, F. Delfanian, T. Letcher, Failure Analysis and Mechanical Characterization of 3D Printed ABS With Respect to Layer Thickness and Orientation, J. Fail. Anal. Prev. 16 (2016) 467–481. doi:10.1007/s11668-016-0113-2.

[14] B.H. Lee, J. Abdullah, Z.A. Khan, Optimization of rapid prototyping parameters for production of flexible ABS object, J. Mater. Process. Technol. 169 (2005) 54–61. doi:10.1016/j.jmatprotec.2005.02.259.

[15] G. Domínguez-Rodríguez, J.J. Ku-Herrera, A. Hernández-Pérez, An assessment of the effect of printing orientation, density, and filler pattern on the compressive performance of 3D printed ABS structures by fuse deposition, Int. J. Adv. Manuf. Technol. 95 (2018) 1685–1695. doi:10.1007/s00170-017-1314-x.

[16] E.B. Duoss, T.H. Weisgraber, K. Hearon, C. Zhu, W. Small IV, T.R. Metz, J.J. Vericella, H.D. Barth, J.D. Kuntz, R.S. Maxwell, C.M. Spadaccini, T.S. Wilson, Three-dimensional printing of elastomeric, cellular architectures with negative stiffness, Adv. Funct. Mater. 24 (2014) 4905–4913. doi:10.1002/adfm.201400451.

[17] T.H. Weisgraber, E.B. Duoss, T.S. Wilson, A mechanical reduced order model for elastomeric 3D printed architectures, 2017.

[18] Y. Jin, J. Plott, A. Shih, Extrusion-based additive manufacturing of the moisture-cured silicone elastomer, Proc. Solid Free. Fabr. Symp. (2015) 308–318. doi:10.1017/CBO9781107415324.004.

[19] K.B. Putra, J. Plott, A.J. Shih, Biaxial Mooney-Rivlin Coefficient of Silicone Sheet by Additive Manufacturing, Procedia CIRP. 65 (2017) 189–195. doi:10.1016/j.procir.2017.04.049.

[20] K. Qiu, Z. Zhao, G. Haghiashtiani, S.Z. Guo, M. He, R. Su, Z. Zhu, D.B. Bhuiyan, P.

Murugan, F. Meng, S.H. Park, C.C. Chu, B.M. Ogle, D.A. Saltzman, B.R. Konety, R.M. Sweet, M.C. McAlpine, 3D Printed Organ Models with Physical Properties of Tissue and Integrated Sensors, Adv. Mater. Technol. 3 (2018) 1–9. doi:10.1002/admt.201700235.

[21] T.H. Kwon, F. Shen, K.K. Wang, Pressure Drop of Polymeric Melts in Conical Converging Flow: Experiments and Predictions, Polym. Eng. Sci. 26 (1986).

[22] R. Brown, Physical test methods for elastomers, 2017. doi:10.1007/978-3-319-66727-0.

[23] A. International, ASTM C365 / C365M-11a, Standard Test Method for Flatwise Compressive Properties of Sandwich Cores, West Conoshoken, PA, 2011. doi:10.1520/C0365.

[24] C. Keplinger, T. Li, R. Baumgartner, Z. Suo, S. Bauer, Harnessing snap-through instability in soft dielectrics to achieve giant voltage-triggered deformation, Soft Matter. 8 (2012) 285–288. doi:10.1039/c1sm06736b.

[25] C. Findeisen, J. Hohe, M. Kadic, P. Gumbsch, Characteristic of mechanical metamaterials based on buckling elements, J. Mech. Phys. Solids. 102 (2017) 151–164.

[26] L.T. Sin, Chapter 5 - Mechanical Properties of Poly(Lactic Acid), in: Polylactic Acid PLA Biopolym. Technonlogy Appl., 1st ed., William Andrew, 2012.

[27] P. Hiemenz, T. Lodge, Networks, Gels and Rubber Elasticity, in: Polym. Chem., Second Edi, CRC Press, 2007: p. 404.

[28] F. Schneider, T. Fellner, J. Wilde, U. Wallrabe, Mechanical properties of silicones for MEMS, J. Micromechanics Microengineering. 18 (2008). doi:10.1088/0960-1317/18/6/065008.

[29] S.-H. Ahn, M. Montero, D. Odell, S. Roundy, P. Wright, Anisotropic material properties of fused deposition modeling ABS, Rapid Prototyp. J. 8 (2002) 248–257. doi:10.1016/S0753-9053(97)80025-7.

Appendix A: Uncertainty Analysis

The measurement uncertainty of the relative density is reported as a combined standard uncertainty with a 95% confidence interval. The uncetainity in measured dimensions is estimated to be 0.3 mm due to the flexibility of the samples. This is error is much greater than the resolution of the calipers used to measure the dimensions (0.01 mm), so the resolution is ignored.

The formula for the relative density:

$$R = \frac{\rho_{sample}}{\rho_{bulk}}$$

Where ρ is the density and the subscript denotes the foam sample or bulk material. The bulk density is 1.04 g/mL as per the manufacturer data sheet.

The combined standard uncertainty is determined by summation in quadrature. First the uncertainty in the measurement of the volume, given by the formula:

$$\frac{u(V)}{V} = \sqrt{\left(\frac{u(l)}{l}\right)^2 + \left(\frac{u(w)}{w}\right)^2 + \left(\frac{u(h)}{h}\right)^2}$$

Where *u*(x) represents the uncertainty of x and l, w, h are the lengths, widths and height measurements, respectively.

A similar procedure is used to calculate the uncertainty in the relative density, and the manufacturer value for the density is assumed to be accurate.

The relative density of the entire sample will be dependent on the number of perimeters and sample size. To account for this effect, the perimeters and shells are subtracted from the overall mass. The compression samples have two top and bottom shells, and 2 perimeter walls.

And for partial walls,

$$V = 2 \cdot (l - 2 \cdot 0.82) \cdot w \cdot h$$

Since 0.82 mm is the wall thickness and there are walls on both sides. The total perimeter volume is 1028 mm^3.

There are four top and bottom shells, with a total volume of 3431 mm^3. Thus the total non-infill volume is 4559 mm^3 or ~4.6 mL. The total volume of the part is 12.8 mL, thus the infill volume is 8.2 mL and the total. The mass to be subtracted to account for the perimeters and shells is 4.78 g.

A 10 x10 x 4 mm sample is cut from the gauge section of the tensile bars after testing. An analysis similar to that of the compression samples is performed and the total mass to be subtracted from the total mass is 0.068 grams.

Appendix B: Printhead Velocity Calibration

Verification of printhead velocity was performed by measuring the time for the printhead to traverse two perimeters of a 10 x10 cm square path (800 mm total) with a handheld stopwatch.

Trial	Time (s)	Velocity (mm/s)
1	13.93	57
2	13.60	59
3	13.69	58
Average	13.74	58

The average value of 58 mm/s closely matches that of the set value of 60 mm/s when accounting for human error in measurement and the non-constant velocity due to cornering.

Appendix C: Firmware Settings

The firmware used in this study is Marlin 1.3.x. Newer versions are available and results may vary.

Table B.1: Firmware settings

Setting	Value
Velocity (v)	60 mm/s (200 mm/s fast travel)
Acceleration (a)	1000 mm/s^2
Jerk*	200 mm/s^2
Slice height (h)	300
Seam Position	Random
Default Extrusion Width	410 (=nozzle diameter)

*Note that jerk here is not the physical definition of jerk (i.e. the third derivative of position vs. time with respect to time), rather a "vector jerk" as defined in the Marlin firmware. See MarlinFW.org for a detailed explanation.